

Molecular Physics: An International Journal at the Interface Between Chemistry and Physics

Publication details, including instructions for authors and subscription information:

<http://www.tandfonline.com/loi/tmph20>

The melting point of lithium: an orbital-free first-principles molecular dynamics study

Mohan Chen^a, Linda Hung^b, Chen Huang^c, Junchao Xia^a & Emily A. Carter^{a,d}

^a Department of Mechanical and Aerospace Engineering, Princeton University, Princeton, New Jersey, 08544, USA

^b Laboratoire des Solides Irradiés École Polytechnique, CNRS, CEA-DSM, F-91128, Palaiseau, France

^c Theoretical Division, T-1, Los Alamos National Laboratory, New Mexico, 87544, USA

^d Andlinger Center for Energy and the Environment and Program in Applied and Computational Mathematics, Princeton University, Princeton, New Jersey, 08544, USA

Published online: 25 Aug 2013.

To cite this article: Molecular Physics (2013): The melting point of lithium: an orbital-free first-principles molecular dynamics study, Molecular Physics: An International Journal at the Interface Between Chemistry and Physics, DOI: 10.1080/00268976.2013.828379

To link to this article: <http://dx.doi.org/10.1080/00268976.2013.828379>

PLEASE SCROLL DOWN FOR ARTICLE

Taylor & Francis makes every effort to ensure the accuracy of all the information (the "Content") contained in the publications on our platform. However, Taylor & Francis, our agents, and our licensors make no representations or warranties whatsoever as to the accuracy, completeness, or suitability for any purpose of the Content. Any opinions and views expressed in this publication are the opinions and views of the authors, and are not the views of or endorsed by Taylor & Francis. The accuracy of the Content should not be relied upon and should be independently verified with primary sources of information. Taylor and Francis shall not be liable for any losses, actions, claims, proceedings, demands, costs, expenses, damages, and other liabilities whatsoever or howsoever caused arising directly or indirectly in connection with, in relation to or arising out of the use of the Content.

This article may be used for research, teaching, and private study purposes. Any substantial or systematic reproduction, redistribution, reselling, loan, sub-licensing, systematic supply, or distribution in any form to anyone is expressly forbidden. Terms & Conditions of access and use can be found at <http://www.tandfonline.com/page/terms-and-conditions>

RESEARCH ARTICLE

The melting point of lithium: an orbital-free first-principles molecular dynamics study

Mohan Chen^a, Linda Hung^b, Chen Huang^c, Junchao Xia^a and Emily A. Carter^{a,d,*}

^aDepartment of Mechanical and Aerospace Engineering, Princeton University, Princeton, New Jersey 08544, USA; ^bLaboratoire des Solides Irradiés École Polytechnique, CNRS, CEA-DSM, F-91128 Palaiseau, France; ^cTheoretical Division, T-1, Los Alamos National Laboratory, New Mexico 87544, USA; ^dAndlinger Center for Energy and the Environment and Program in Applied and Computational Mathematics, Princeton University, Princeton, New Jersey 08544, USA

(Received 22 May 2013; accepted 15 July 2013)

The melting point of liquid lithium near zero pressure is studied with large-scale orbital-free first-principles molecular dynamics (OF-FPMD) in the isobaric-isothermal ensemble. We adopt the Wang-Govind-Carter (WGC) functional as our kinetic energy density functional (KEDF) and construct a bulk-derived local pseudopotential (BLPS) for Li. Our simulations employ both the ‘heat-until-melts’ method and the coexistence method. We predict 465 K as an upper bound of the melting point of Li from the ‘heat-until-melts’ method, while we predict 434 K as the melting point of Li from the coexistence method. These values compare well with an experimental melting point of 453 K at zero pressure. Furthermore, we calculate a few important properties of liquid Li including the diffusion coefficients, pair distribution functions, static structure factors, and compressibilities of Li at 470 K and 725 K in the canonical ensemble. Our theoretically-obtained results show good agreement with known experimental results, suggesting that OF-FPMD using a non-local KEDF and a BLPS is capable of accurately describing liquid metals.

Keywords: orbital-free density functional theory; molecular dynamics; melting temperature; liquid lithium; superheating effect

1. Introduction

The Li phase diagram has garnered broad interest in recent years, as evidenced by both experimental [1,2] and theoretical [3,4] studies. At ambient conditions, solid Li has a body-centred cubic (bcc) structure and melts at 453 K [5]. The resulting liquid Li shows promise in applications involving plasma-facing materials [6] used for components of fusion reactors that must withstand a high flux of high-energy particles. Such applications using liquid Li require a better understanding of the melting point of solid Li, as well as properties of liquid Li such as its diffusion coefficients and its interactions with high-energy particles (e.g., deuterium).

Several computational methods can be used to theoretically estimate the melting point of materials under fixed pressure and temperature [7]. The simplest and most straightforward simulation approach is the ‘heat-until-melts’ method. Here, the temperature of the simulation cell is raised until the solid phase of a material melts. The melting temperature obtained from this method is often called the ‘mechanical melting point’. A drawback of this method is that the model can only provide an upper bound for the actual melting point due to superheating effects. Although the superheating effect is claimed to be low in alkali metals such as Li [8] and Na [9], further study is needed. An alter-

native method is to directly simulate the coexistence of solid and liquid phases [10,11]. This approach typically requires a larger simulation cell. Since these two-phase simulations are therefore more computationally demanding, most are run using classical potentials [10]; however, first-principles methods have been used in some recent work for Al [12,13] and Li [3]. A third option is to calculate the Gibbs free energy of both the solid and liquid phases [14–16]. The melting line can then be estimated as the temperature at which the Gibbs free energies from the two phases are equal. The disadvantage to this method is that free energy calculations are nontrivial and require a very high accuracy to be meaningful.

First-principles calculations have played an important role in the discovery of new structures [17] and in improving phase diagrams for Li [3,4]. Orbital-free density functional theory (OFDFT) is a first-principles method based on the Hohenberg–Kohn theory [18] and uses a sole variable, the electron density, to obtain the system energy.

Several features of OFDFT make it far more computationally efficient than the conventional Kohn–Sham density functional theory (KSDFT) [18,19]. First, wave functions are not used in OFDFT, so their orthogonalisation can be avoided. Second, *k*-point sampling is not needed. Finally, OFDFT has $O(MnN)$ (here, *N* is the number of atoms)

*Corresponding author. Email: eac@princeton.edu

scaling for all systems including metals. With these computational advantages, OFDFT can be a powerful tool when used within molecular dynamics.

However, by completely avoiding wave functions in an OFDFT formalism, there are some tradeoffs in accuracy relative to KSDFT that must be addressed. First, an accurate kinetic energy density functional (KEDF) must be selected. Second, transferable local pseudopotentials must be obtained. We will discuss our choices of KEDF and local pseudopotentials in Section 2. Nevertheless, OFDFT generally has a similar level of accuracy as KSDFT in systems of light metals that have a nearly free-electron-like density. We note that recent developments in our group have also extended the capabilities of OFDFT to treat covalently bonded systems [20,21] and transition metals [22].

Although several OF-FPMD studies have been used to model light metals such as Li, Na, Al, etc. over the past two decades [12,23–27], most simulations were limited to the microcanonical ensemble NVE (with a constant number of particles N , constant volume V , and constant energy E). Ensembles such as the canonical ensemble and the isothermal-isobaric ensemble are highly useful for studying material properties under different environments, so in our study, we use the isothermal-isobaric ensemble to estimate the melting temperature of Li using OF-FPMD.

The outline is as follows. The methodology for the OF-FPMD implementation is introduced in Section 2. Our results and discussion are presented in Section 3. There, we discuss more details about the ‘heat-until-melts’ method (Section 3.1), which can only provide an upper bound of the melting point of Li. We study systems ranging from 128 to 1024 atoms to eliminate size effects. We also discuss more details about the coexistence method (Section 3.2), which gives an accurate estimate of the melting temperature. Several other additional material properties are also calculated in Section 3.3, including diffusion coefficients, pair distribution functions, static structure factors, and compressibilities. These properties are calculated in the canonical ensemble at selected temperatures. Finally, conclusions are made in Section 4.

2. Methods

OF-FPMD simulations were run using our own PRinceton Orbital-Free Electronic Structure Software (PROFESS) program. Detailed implementation and performance information can be found in references [28–30]. As mentioned in the introduction, two approximations in OFDFT must be carefully made to ensure accuracy. The first approximation is the form of the KEDF. Modern KEDF theory adopts the non-local form that has been continuously developed by several groups [31–36]. The present study reports simulation data using the Wang–Govind–Carter (WGC) [36] functional. The WGC KEDF $T_s^{\alpha\beta\gamma}$ is written as a functional

of electron density $\rho(\mathbf{r})$ and consists of three terms,

$$T_s^{\alpha\beta\gamma}[\rho(\mathbf{r})] = T_{TF}[\rho(\mathbf{r})] + T_{vW}[\rho(\mathbf{r})] + T_{WGC}^{\alpha\beta\gamma}[\rho(\mathbf{r})], \quad (1)$$

where the first term is Thomas–Fermi KEDF [37–39],

$$T_{TF}[\rho(\mathbf{r})] = \frac{3}{10}(3\pi^2)^{\frac{2}{3}} \int_{\Omega} \rho(\mathbf{r})^{\frac{5}{3}} d\mathbf{r}, \quad (2)$$

where Ω is the volume of cell. The Thomas–Fermi KEDF is exact in the limit of the uniform electron gas. The second term is the von Weizsäcker KEDF [40] written as

$$T_{vW}[\rho(\mathbf{r})] = \frac{1}{8} \int_{\Omega} \frac{|\nabla \rho(\mathbf{r})|^2}{\rho(\mathbf{r})}. \quad (3)$$

The von Weizsäcker KEDF is exact for any single orbital system. The third term

$$T_{WGC}^{\alpha\beta\gamma}[\rho(\mathbf{r})] = \frac{3}{10}(3\pi^2)^{\frac{2}{3}} \int \int d\mathbf{r} d\mathbf{r}' \rho^{\alpha}(\mathbf{r}) w_{\alpha\beta} \times [\xi_{\gamma}(\mathbf{r}, \mathbf{r}'), \mathbf{r} - \mathbf{r}'] \rho^{\beta}(\mathbf{r}') \quad (4)$$

is the WGC non-local KEDF term, where $w_{\alpha\beta}(\xi_{\gamma}(\mathbf{r}, \mathbf{r}'), \mathbf{r} - \mathbf{r}')$ is the WGC kernel. The density dependent term is $\xi_{\gamma}(\mathbf{r}, \mathbf{r}') = [\frac{k_F^{\gamma}(\mathbf{r}) + k_F^{\gamma}(\mathbf{r}')}{2}]^{1/\gamma}$ with $k_F = [3\pi^2 \rho(\mathbf{r})]^{1/3}$ the Fermi wave vector. However, the density dependence of the kernel $\xi_{\gamma}(\mathbf{r}, \mathbf{r}')$ makes it impossible to directly use the fast Fourier transform (FFT) to evaluate the non-local KEDF. A second-order Taylor expansion of the WGC kernel is therefore used, so FFTs can be applied to integrate the non-local KEDF and the scaling remains $O(M \ln N)$. The universal parameters of WGC are set to $\alpha = \frac{5}{6} + \frac{\sqrt{5}}{6}$, $\beta = \frac{5}{6} - \frac{\sqrt{5}}{6}$ from asymptotic analysis [36]. The tuning parameter is set to $\gamma = 2.7$, which is found to be optimal for Al [36], and is also suitable for Li.

The second approximation is the derivation of a local pseudopotential. We use the form of a bulk-derived local pseudopotential (BLPS) developed by Carter and co-workers [41,42]. This scheme produces a transferable local pseudopotential via inverting Kohn–Sham equations on the valence electron densities of a few reference bulk crystals. This method [42] employs a direct maximisation of a functional W developed by Wu and Yang [43]

$$W[v_{eff}(\mathbf{r}), \rho_0(\mathbf{r})] = T_s[v_{eff}(\mathbf{r})] + \int d\mathbf{r} [\rho(\mathbf{r}) - \rho_0(\mathbf{r})] v_{eff}(\mathbf{r}), \quad (5)$$

where T_s is the kinetic energy and $v_{eff}(\mathbf{r})$ is the KS effective potential that contains the target BLPS. The electron density from a given reference system is $\rho_0(\mathbf{r})$, while $\rho(\mathbf{r})$ is the electron density during optimisation. Here we use body-centred cubic (bcc), face-centred cubic (fcc), simple

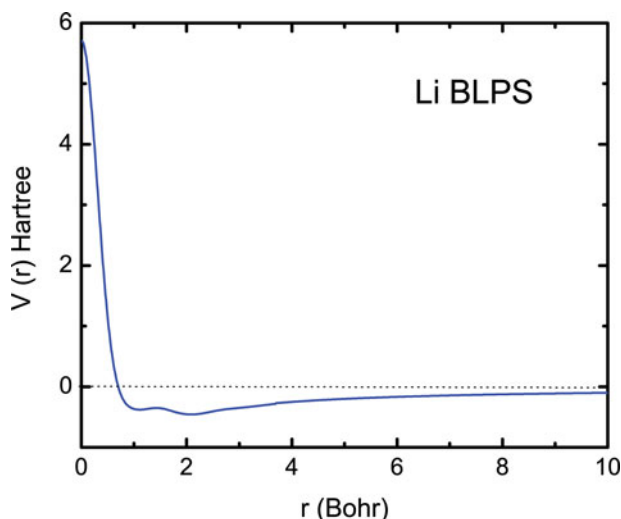


Figure 1. Bulk derived local pseudopotential (BLPS) for Li in real space. The body-centred cubic (bcc), face-centred cubic (fcc), simple cubic (sc), and cubic diamond (dia) structures are used as reference systems.

cubic (sc), and cubic diamond structures as reference systems. We calculate the reference systems from KSDFT using the projector augmented-wave method (PAW) [44–46]. The exchange-correlation functional is described by the generalised-gradient approximation (GGA) in the Perdew, Burke, Ernzerhof (PBE) form [47], which should provide a better estimate for the melting temperature than the local density approximation (LDA) [3,48]. The resulting BLPS of Li is plotted in Figure 1.

We also validate the Li BLPS for a few different crystal phases to ensure it leads to correct energy ordering, lattice constants, and bulk moduli, with results shown in Table 1.

Table 1. Comparison of bulk properties for the body-centred cubic (bcc), face-centred cubic (fcc), simple cubic (sc), and cubic diamond (dia) structures of Li. The PBE exchange-correlation functional is used for all calculations. V_0 is the equilibrium volume. B is the bulk modulus. E is the relative energy per atom with respect to the energy of the bcc structure. KSDFT-PAW results are from VASP [45] calculations using the PAW method. KSDFT-BLPS results are from ABINIT [57] calculations using our Li BLPS. OFDFT results are from PROFESS using our Li BLPS.

Method	Structure	$V_0(\text{\AA}^3)$	B (GPa)	E (eV)
KSDFT-PAW	bcc	20.354	14	0.000
	fcc	20.318	14	−0.002
	sc	20.509	12	0.121
	dia	25.798	5	0.394
KSDFT-BLPS	bcc	20.199	16	0.000
	fcc	20.258	16	−0.001
	sc	21.884	13	0.150
	dia	30.655	6	0.426
OFDFT	bcc	20.207	16	0.000
	fcc	20.266	16	−0.001
	sc	21.948	13	0.150
	dia	30.328	6	0.427

There, we compare OFDFT results using the WGC KEDF and the Li BLPS to KSDFT using either PAW or the Li BLPS. Although bcc is the expected ground state structure, the simulation results all indicate that the fcc structures have the lowest energies. However, the energies of bcc structures lie only 1–2 meV/atom above the fcc energies, suggesting the bcc and fcc energies are almost degenerate. The energy ordering between bcc and other structures are well captured by all calculations.

The Murnaghan’s equation of state [49] is used to calculate the bulk moduli. The bulk moduli and the equilibrium volumes from KSDFT-BLPS and OFDFT are in perfect agreement, showing the high quality of the WGC KEDF. Larger deviations appear when comparing KSDFT-PAW calculations to calculations using the BLPS, although all results are still in good agreement. Simulations with both KSDFT-BLPS and OFDFT predict slightly larger bulk moduli than KSDFT-PAW, but results differ only up to 2 GPa. The equilibrium volumes for bcc and fcc match well for all three methods, which is important in this study because we choose bcc as the crystal structure of solid Li (appropriate under ambient conditions). Larger deviations of equilibrium volumes exist in sc and diamond structures but we find these have little effect on our results presented below.

For the molecular dynamics simulations, periodic boundary conditions are used. We choose a high kinetic energy cutoff of 900 eV, which converges the energy per atom to 4.0×10^{-3} meV in the bcc structure. To efficiently calculate the ion–ion and ion–electron interactions, we use the cardinal B-spline method (see Ref. [29,30] and references therein), which has $O(MnN)$ scaling. At each time step, the electron density is fully optimised to stay on the Born–Oppenheimer surface. As a criterion for convergence, we set the tolerance of potential differences to 10^{-6} hartree in PROFESS, which prevents drift of conserved quantities during the MD simulation. Six or seven electronic energy iterations are typically required for each time step.

Three major ensembles are now implemented in the PROFESS code: the microcanonical ensemble NVE (constant number of particles N , constant volume V , and constant energy E), the canonical ensemble NVT (constant number of particles N , constant volume V , and constant temperature T) and the isothermal-isobaric ensemble NPT (constant number of particles N , constant pressure P , and constant temperature T). Specifically, we adopt the Nosé–Hoover thermostat [50,51] for NVT dynamics and the Parrinello–Rahman baro-thermostat [52] for NPT dynamics. Detailed algorithms can be found in work by Martyna, *et al.* [53]. Currently, the Nosé–Hoover chain method has not been implemented in PROFESS.

Simulations reported in this paper use time steps of 0.1 fs with time intervals of 2.5 fs to evaluate all the quantities, including pair distribution functions and static structure factors. We find that the thermostat mass has little effect on the final results unless very small values are chosen. We

therefore choose a Nosé–Hoover thermostat mass of 5×10^3 au and a barostat mass of 2.5×10^7 au in the 128-atom system, and increase the mass linearly with atom number up to the 1024-atom system. Initial velocities sample a Maxwell–Boltzmann distribution. Some benchmarks were run on 2.6 GHz Intel Xeon E5-2670 processors. The speed of PROFESS is remarkable. For example, for an 8-processor run on 128 atoms, each MD step takes around 2 seconds. For a 16-processor run on a 512-atom system, each MD step takes around 5 seconds.

3. Results and discussion

3.1. Heat-until-melts method

The ‘heat-until-melts’ method involves simulating a solid material at increasing temperatures until the phase transition to liquid is observed. As mentioned in the introduction, this method overestimates transition temperature because of well-known superheating effects, and thus such simulations only provide an upper bound to the melting temperature [54].

Density-temperature curves obtained from ‘heat-until-melts’ simulations are shown in Figure 2. Since the crystal structure of Li near zero pressure is bcc, we use this crystal structure for our solid. Because the volume of the cell should increase during heating, the density of Li is expected to decrease with increasing temperature. At the melting point, the density should decrease abruptly, indicative of a first-order phase transition.

Our NPT simulations show the expected behaviour, as illustrated in Figure 2. The red solid line (128-atom cell) shows a linear decrease in density starting from 200 K

onward. The density sharply drops down at 449 K and then continues decreasing linearly as the temperature increases. This drop indicates a phase transition from solid to liquid and can be easily confirmed by observing the geometries such as those shown in the insets of Figure 2. Both cell snapshots are taken after the system evolves for 15 ps to reach equilibrium and then is equilibrated for another 15 ps. The inset with atoms in blue at 440 K shows atoms fluctuating around their equilibrium positions in a bcc structure, while the inset with atoms in pink that are disordered, as expected in the liquid structure. The mechanical melting temperature is therefore 449 K in the 128-atom cell.

To study the cell size effect of the mechanical melting temperature, we also modelled larger 256- and 1024-atom cells and find the melting temperature is 464 K for the 256 atom case and 465 K for the 1024-atom system. Thus, our results show that the cell size effect for Li is already negligible for the 256-atom cell. To our surprise, the mechanical melting temperatures from ‘heat-until-melts’ simulations are in good agreement with the experimental value of 453 K [5]. This implies that ‘heat-until-melts’ simulations appear suitable to study the melting of Li.

3.2. Coexistence method

The coexistence method has been used with many classical potentials [10], but due to its large computational cost, it has been rarely used with first-principles based simulations. These simulations require a large cell. In past work [3,13], researchers reported that at least 500 atoms are needed to construct a reliable solid–liquid interface. We tested two cells containing either 256 or 512 atoms. As expected, we could hardly observe any phase coexistence in the 256-atom system.

We now report a procedure to build a reliable interface structure for 512-atom cells. Note that great care must be taken to produce an equilibrium state of phase coexistence that does not disrupt the original solid and liquid phases [55].

First, we prepare solid and liquid phases separately, each in simulation cells containing 256 atoms. We choose densities near the melting point for both the solid and liquid phases: 0.0456 \AA^{-3} for the solid phase and 0.0442 \AA^{-3} for the liquid phase (see Figure 2). We set the interface by joining these two phases along the z -direction, and choose the same xy cross section for both phases. The cell for the solid phase is $14.107 \times 14.107 \times 28.214 \text{ \AA}$, while the cell for the liquid phase is $14.107 \times 14.107 \times 29.098 \text{ \AA}$. Note that a longer cell distance in the z -direction yields a smaller density.

Next, molecular dynamics simulations are carried out for the separate solid (at 440 K) and liquid (at 470 K) systems with the Nosé–Hoover thermostat for 10 ps, which results in well-defined solid and liquid phase structures. Mean square displacement (MSD) is useful here, which is

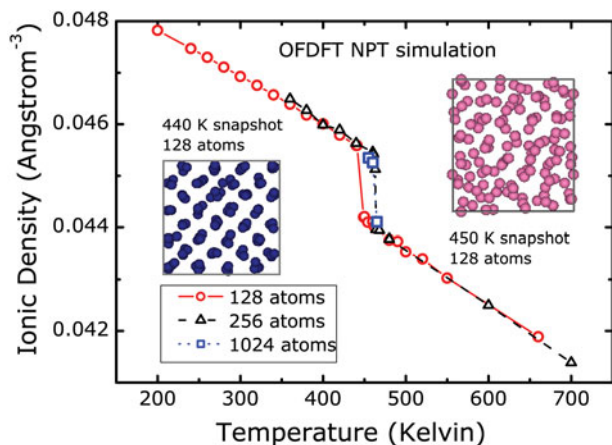


Figure 2. Density-temperature curve for Li, using simulation cells containing different numbers of atoms. Each point corresponds to an NPT simulation. The external pressure is fixed at zero. The estimated mechanical melting temperature is 449K, 464K, and 465K for 128, 256, and 1024 atoms, respectively. The insets show simulation snapshots of cells at 440 K (left inset, atoms in blue) and 450 K (right inset, atoms in pink) after the system has been in the equilibrium for 15 ps.

defined as $u^2(t)$ according to

$$u^2(t) = \frac{1}{N} \sum_{i=1}^N [R_i(t) - R_i(0)]^2, \quad (6)$$

where $R_i(t)$ is the atom position of atom i after t time of simulation. N is the total number of atoms. The MSD provides the means to observe whether the system is in a solid or liquid state. If the system stays in the solid state, the MSD oscillates around a constant value. This indicates that all the atoms are confined to certain positions. However, if some of the atoms melt, the MSD linearly increases. We monitor the geometry and MSD to ensure that the solid remains in a bcc structure, while the liquid retains a good pair-distribution function shape.

We then join the two structures together along the z -direction. In this case, the interface structure for the bcc solid is the (001) surface. Because the xy cross sections are the same for the two phases, the total unit cell is now $14.107 \times 14.107 \times 57.312$ Å. Now the cell has two solid-liquid interfaces due to the periodic boundary conditions. Despite the care taken in constructing the interface, this new phase coexistence structure is still far from stable. The liquid phase still must be equilibrated next to the solid phase. Otherwise, at the start of molecular dynamics simulations, this high-energy interface will likely be destroyed. To stabilise this interface in the solid phase, we average the solid phase atomic positions from 0.25 ps of previous separate solid-phase calculations. Due to the periodic boundary conditions and the fluctuations of solid atoms, some neighbouring atoms in the solid phase may become separated by more than one cell length, so one should ensure that no vacancies are accidentally created at the solid-liquid surface. To decrease the interface energy on the liquid side, we fix the solid atom positions and relax the liquid structure at a chosen temperature for less than 1 ps. We choose the temperature to be 450 K, which we expect to be near the calculated melting temperature. This step is done with an NVT simulation. We find that the energy of the system decreases quickly at first and then fluctuates around a constant value.

Finally, an NPT simulation is carried out to allow both the density and the atom positions of the two-phase system to relax. For different temperatures, we use the same starting geometry but scale the initial velocities to the target temperature. If the starting temperature is too low, some liquid atoms solidify. Conversely, if the starting temperature is too high, some solid atoms liquify. Since the ‘heat-until-melts’ method determined the upper limit of Li melting to be at 465 K, we sample temperatures between 370 K and 470 K. For every 10 K, we monitor the geometry and the MSD. Below 430 K, all liquid-phase atoms freeze within a few ps. Above 440 K, all solid-phase atoms spontaneously melt. This allows us to refine our best estimate for the melting temperature to be between 430 K and 440 K. We then

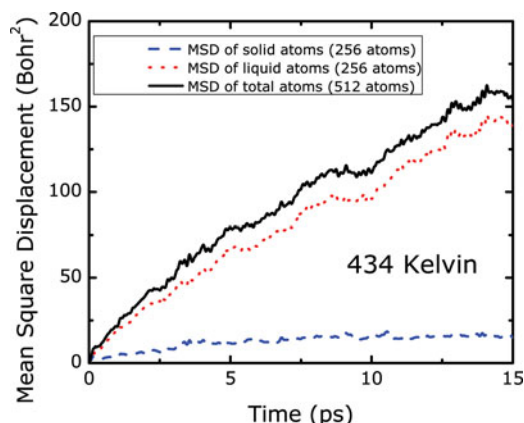


Figure 3. The mean square displacement (MSD) for the coexistence structure of solid and liquid phases at 434 K. Black solid line is the MSD for all the 512 atoms in this structure. The red dotted line is the MSD for the 256 atoms initialised as liquid, while the blue dashed line is the MSD for the atoms initialised as solid.

further decrease the temperature interval to as small as 1 K and carry out NPT simulations again. From these results, we find that phase coexistence is extremely sensitive to the temperature and exists only around 434 K.

Figure 3 shows our plot for the MSD at 434 K for the solid and liquid atoms separately and demonstrates the phase coexistence. The blue dashed line in Figure 3 clearly shows the MSD for the solid phase, which slightly increases at the beginning of the run and then oscillates around a constant value. In contrast, the liquid phase (dotted red line) has a larger and linearly-increasing MSD, clearly indicating its fluidity. Figure 4 helps us to further understand the results. Figure 4(a) shows the initial geometry, where the solid atoms are in blue and the liquid atoms are in pink. Figure 4(b) is a snapshot at 5 ps that shows a few atoms (coloured pink) originally in the liquid phase change positions with atoms (coloured blue) originally in the solid phase. The melted blue atoms contribute to the MSD of blue atoms as a whole. Finally Figure 4(c) shows that the solid and liquid phase are well separated even after 15 ps, confirming the coexistence of solid and liquid phases. Figure 5 shows the profile of liquid and solid atoms at the beginning of the simulation and after 15 ps. The liquid phase atoms are always more uniformly distributed than the solid atoms. Moreover, in Figure 5(b) we find the ionic density in the solid-liquid interfaces are more smoothly connected after 15 ps, while the two phases are still clearly divided. Based on these simulations, we conclude that 434 K should be the melting temperature of Li. This value is 31 K lower than the mechanical melting temperature (as expected since the latter is an upper bound) and remarkably only 19 K below the known experimental value 453 K [5]. Our prediction is also 21 K lower than that from a KSDFT simulation [3], suggesting that some very small errors remain in the BLPS and the KEDF. Some systematic errors may also exist due

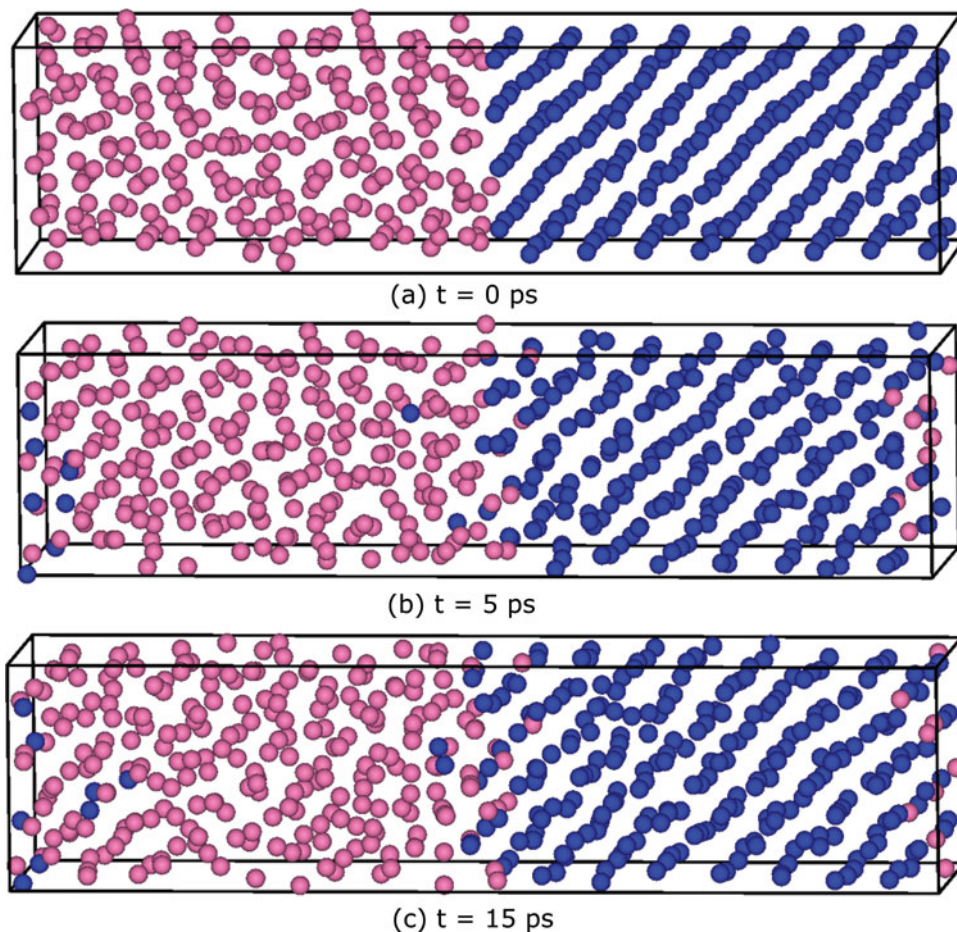


Figure 4. The geometries for the coexistence structure of solid (blue) and liquid (pink) phases at 434 K. (a) Initial geometry. (b) Geometry after 5 ps of NPT. (c) Geometry after 15 ps of NPT.

to fluctuations of the interface size [56]. However, in our simulations we expect this source of error to be small because our initial lattice constant for solid Li is equilibrated at 440 K, which is very close to the target melting temperature of 434 K.

3.3. Static and dynamic properties

To provide further insight into the properties of liquid Li, we compare its static and dynamic properties to measurements. We extract the density values for Li from Figure 2 at 470 K and 725 K. NVT simulations are run at these fixed densities. We use these densities instead of experimental values, since the latter subject the cell to a larger stress, which may affect the calculated properties. Detailed values are listed and compared to experimental and theoretical references in Table 2. The ionic density is 0.0439 \AA^{-3} at 470 K, which is 1.34% smaller than the experimental value. Also, the ionic density is 0.0412 \AA^{-3} at 725 K, which is 3.19% smaller than the experimental value. These values are reasonable since our ground state PBE OFDFT calculations of bcc Li yield a slightly smaller lattice constant compared to experiments.

The external pressure P is calculated by $p = (p_x + p_y + p_z)/3$, where the p_x , p_y , and p_z are the diagonal components of the stress tensor. Our external pressures are

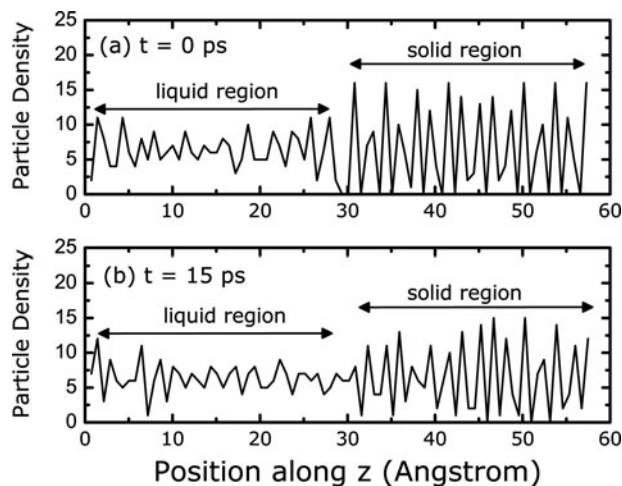


Figure 5. The ionic density profiles for the coexistence structure of solid and liquid phases at 434 K. (a) Initial ionic density profile. (b) Ionic density profile after 15 ps of NPT.

Table 2. Detailed properties of liquid Li. Our simulations are labelled OF-AIMD(WGC+BLPS), while OF-AIMD(A) and OF-AIMD(B) are results of OFDFT MD simulations by Anta and Madden [24]. Here A and B refers to two different pseudopotentials. The simulation results labelled KS-AIMD are by Kresse [58]. The experimental data are from reference [59]. Number of atoms N , temperature T , ionic density ρ , external pressure P , compressibility χ_T and diffusion coefficient D are listed.

	N	T/K	ρ / kgm^{-3}	P/MPa	$\chi_T/10^{-4}\text{MPa}^{-1}$	$D/\text{\AA}^2\text{ps}^{-1}$
OF-AIMD(WGC+BLPS)	128	470	506.4	240 ± 120	1.10	0.63 ± 0.04
OF-AIMD(A)	479	470	513.4	1400	0.98	0.82 ± 0.05
OF-AIMD(A)	176	470	513.4	1420	1.41	0.76 ± 0.05
OF-AIMD(B)	176	470	513.4	-2600	1.13	0.55 ± 0.05
KS-AIMD	128	470				0.69
Experiment		470	513.4	~ 0	1.02	0.63
OF-AIMD(WGC+BLPS)	128	725	474.6	350 ± 180	1.56	2.21 ± 0.03
OF-AIMD(A)	128	725	491.0	1380	2.09	1.78 ± 0.05
Experiment		725	491.0	~ 0	1.20	1.79

around 300 MPa, which are four or five times smaller than in Anta's and Madden's simulations [24]. This large difference is due to our choice to employ OF-FPMD-optimised lattice constants in our simulation, while Anta's and Madden's calculations were based on the experimental ionic density, resulting in a larger external pressure. Our calculated pressure is not totally zero, possibly because the ionic density in Figure 2 is from a statistical average. However, we find this small value of external pressure does not affect our calculated results.

We find that the off-diagonal components of the stress tensor fluctuate around zero, indicating zero shear stress on the cell. We use 15 ps of equilibrium configurations to calculate diffusion coefficients (Table 2), pair distribution functions (Figure 6), static structure factors (Figure 6) and compressibilities (Table 2) of liquid lithium. We calculate

the diffusion coefficients D as:

$$D = \frac{1}{6} \lim_{t \rightarrow \infty} \frac{u^2(t) - u^2(0)}{t}. \quad (7)$$

As is shown in Table 2, our predicted diffusion coefficient is around $0.63 \text{ \AA}^2\text{ps}^{-1}$ for liquid lithium at 470 K, identical to the experimental value. For the higher temperature of 725 K, OFDFT MD yields a value of $2.21 \text{ \AA}^2\text{ps}^{-1}$, which is larger than the experimental $1.79 \text{ \AA}^2\text{ps}^{-1}$, but still reasonable.

In Figure 6, we show the calculated pair distribution functions and static structure factors $S(k)$ for liquid lithium. The pair distribution functions $g(r)$ are calculated from

$$g(r) = \frac{1}{\rho N} \left\langle \sum_{i=1}^N \sum_{j=1, j \neq i}^N \delta(\mathbf{r} - \mathbf{R}_i + \mathbf{R}_j) \right\rangle, \quad (8)$$

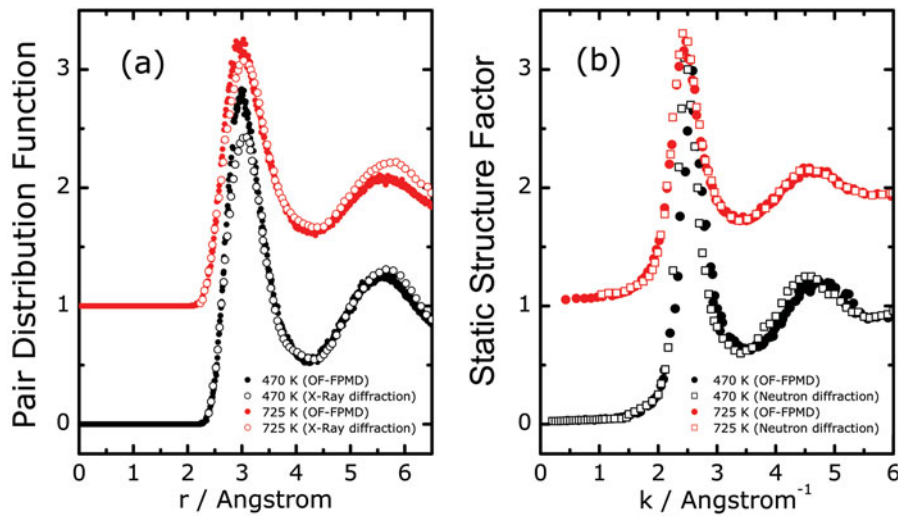


Figure 6. The pair distribution functions (a) and static structure factors (b) of liquid Li at 470 K and 725 K. The simulations with 128 atoms are carried out within the canonical ensemble. The results of 725 K are shifted upwards by unity for ease of viewing. Experimental data are from reference [60].

where here ρ is the ionic density and i, j indicate atoms. The spherically averaged distance between ions is $r = |\mathbf{r}|$. Due to periodic boundary conditions, the average ion-ion distance of the pair distribution function is only determined up to half of the cell length. The static structure factors $S(k)$ are calculated from

$$S(k) = \frac{1}{N} \left\langle \sum_{i=1}^N \sum_{j=1}^N e^{i\mathbf{k}(\mathbf{R}_i - \mathbf{R}_j)} \right\rangle, \quad (9)$$

where \mathbf{k} is the reciprocal space vector of a given cell and the spherically-averaged reciprocal space vector $k = |\mathbf{k}|$. We calculate the static structure factors using Equation (9) instead of obtaining them from a Fourier transform of pair distribution functions, since this eliminates the finite size error introduced by the pair distribution functions.

Overall, we see that the predicted shapes and locations of the peaks of both pair distribution functions and static structure factors match experimental values exceedingly well at both temperatures. Compared to experimental values, the 470 K pair distribution function overestimates the first peak but matches the second peak well. On the other hand, the 725 K pair distribution function matches the first peak well but slightly underestimates the second peak. The 470 K static structure factor shifts very slightly towards larger k values compared to the experiment. However, the 725 K static structure factor matches experimental values nearly perfectly.

We also calculate the value of compressibilities according to

$$\chi_T = \frac{S(0)}{\rho k_B T} \quad (10)$$

where $S(0)$ is the static structure factor at $k = 0$, k_B is the Boltzmann factor, and T is the temperature. Due to limitations on cell size, this value can only be obtained by extrapolation. We use a second-order polynomial and extrapolate the data from small k to $k = 0$. The results are shown in Table 2. The compressibility is $1.10 \times 10^{-4} \text{MPa}^{-1}$ for Li 470 K, which is very close to the experimental value of $1.02 \times 10^{-4} \text{MPa}^{-1}$. Our simulation with 128 atoms exhibits slightly worse performance than Anta's and Madden's OF-AIMD(A) with 479 atoms at 470 K, which yields $0.98 \times 10^{-4} \text{MPa}^{-1}$ [24]. For Li at 725 K, our compressibility is $1.56 \times 10^{-4} \text{MPa}^{-1}$ compared to an experimental value of $1.20 \times 10^{-4} \text{MPa}^{-1}$. These results are superior to Anta's and Madden's OF-AIMD(A) for both 470 K (176 atoms) and 725 K (128 atoms) [24]. This agreement between OFDFT MD and measurements is remarkable, given that OFDFT is a fully first-principles theory that does not incorporate empirical data.

4. Conclusions

We have used orbital-free first-principles molecular dynamics to study the melting temperature of Li near zero pressure

using the isothermal-isobaric ensemble. Two methods have been used: the 'heat-until-melts' method, which gives an upper bound to the melting temperature of 465 K, and the coexistence method, which estimates the melting point of Li to be 434 K. These calculations were made possible due to the newly-implemented molecular dynamics routines that allow different statistical mechanical ensembles to be simulated in PROFESS. Our results compare well with the experimental melting point of 453 K [5]. To further validate our results, we compared experimental and calculated values of diffusion coefficients, pair distribution functions, static structure factors, and compressibilities of Li at 470 K and 725 K. Overall, we find excellent agreement between theory and experiment. Our results prove that when a high-quality, non-local KEDF and an accurate BLPS are employed, the orbital-free density functional theory is an accurate quantum mechanics method that can characterise properties of both solid and liquid Li.

Acknowledgements

It is a pleasure to dedicate this article to Prof Giovanni Ciccotti on the occasion of a special birthday milestone. Long ago, he taught one of us (EAC) everything she knows about molecular dynamics simulations. We thank the Office of Naval Research and the Department of Energy, Fusion Energy Sciences funding for support of this research. We are grateful to Ilgyou Shin, Dr Youqi Ke, Dr Florian Libisch, Joseph Vella, and Prof Athanassios Panagiotopoulos for helpful discussions. We thank Dr John Keith for help in editing this manuscript.

References

- [1] C.L. Guillaume, E. Gregoryanz, O. Degtyareva, M.I. McMahon, M. Hanfland, S. Evans, M. Guthrie, S.V. Sinogeikin, and H.K. Mao, *Nature Phys.* **7**, 211 (2011).
- [2] A.M.J. Schaeffer, W.B. Talmadge, S.R. Temple, and S. Deemyad, *Phys. Rev. Lett.* **109**, 185702 (2012).
- [3] E.R. Hernandez, A. Rodriguez-Prieto, A. Bergara, and D. Alfe, *Phys. Rev. Lett.* **104**, 185701 (2010).
- [4] F.A. Gorelli, S.F. Elatresh, C.L. Guillaume, M. Marques, G.J. Ackland, M. Santoro, S.A. Bonev, and E. Gregoryanz, *Phys. Rev. Lett.* **108**, 055501 (2012).
- [5] R. Boehler, *Phys. Rev. B* **27**, 6754 (1983).
- [6] R. Majeski, L. Berzak, T. Gray, R. Kaita, T. Kozub, F. Levinton, D.P. Lundberg, J. Manickam, G.V. Pereverzev, K. Snieckus, V. Soukhanovskii, J. Spaleta, D. Stotler, T. Strickler, J. Timberlake, J. Yoo, and L. Zakharov, *Nucl. Fusion* **49**, 055014 (2009).
- [7] Y. Zhang and E.J. Maginn, *J. Chem. Phys.* **136**, 144116 (2012).
- [8] I. Tamblyn, J.Y. Raty, and S.A. Bonev, *Phys. Rev. Lett.* **101**, 075703 (2008).
- [9] J.Y. Raty, E. Schwegler, and S.A. Bonev, *Nature* **449**, 448 (2007).
- [10] J.R. Morris, C.Z. Wang, K.M. Ho, and C.T. Chan, *Phys. Rev. B* **49**, 3109 (1994).
- [11] J.R. Morris and X. Song, *J. Chem. Phys.* **116** (21), 9352 (2002).
- [12] B.J. Jesson and P.A. Madden, *J. Chem. Phys.* **113** (14), 5935 (2000).
- [13] D. Alfe, *Phys. Rev. B* **68**, 064423 (2003).

- [14] Q. Sugino and R. Car, Phys. Rev. Lett. **74** (10), 1823 (1995).
- [15] B.J. Jesson and P.A. Madden, J. Chem. Phys. **113** (14), 5924 (2000).
- [16] L. Voadlo and D. Alfe, Phys. Rev. B **65**, 214105 (2002).
- [17] J. Lv, Y. Wang, L. Zhu, and Y. Ma, Phys. Rev. Lett. **106**, 015503 (2009).
- [18] P. Hohenberg and W. Kohn, Phys. Rev. **136**, B864 (1964).
- [19] W. Kohn and L.J. Sham, Phys. Rev. **140**, A1133 (1965).
- [20] C. Huang and E.A. Carter, Phys. Rev. B **81**, 045206 (2010).
- [21] J. Xia and E.A. Carter, Phys. Rev. B **86**, 235109 (2012).
- [22] C. Huang and E.A. Carter, Phys. Rev. B **85**, 045126 (2012).
- [23] M. Foley, E. Smargiassi, and P.A. Madden, J. Phys.: Condens. Matter **6**, 5231 (1994).
- [24] J.A. Anta and P.A. Madden, J. Phys.: Condens. Matter **11**, 6099 (1999).
- [25] D.J. Gonzalez, L.E. Gonzalez, J.M. Lopez, and M.J. Stott, J. Non-Cryst. Solids **312-314**, 110 (2002).
- [26] D.J. Gonzalez, L.E. Gonzalez, and M.J. Stott, Phys. Rev. Lett. **92**, 085501 (2004).
- [27] D.J. Gonzalez, L.E. Gonzalez, and M.J. Stott, Phys. Rev. B **74**, 014207 (2006).
- [28] G.S. Ho, V.L. Ligneres, and E.A. Carter, Comp. Phys. Comm. **179**, 839 (2008).
- [29] L. Hung, C. Huang, I. Shin, G.S. Ho, V.L. Ligneres, and E.A. Carter, Comp. Phys. Comm. **181**, 2208 (2010).
- [30] L. Hung and E.A. Carter, Chem. Phys. Lett. **475**, 163 (2009).
- [31] L.W. Wang and M.P. Teter, Phys. Rev. B **45**, 13196 (1992).
- [32] F. Perrot, J. Phys.: Condens. Matter **6**, 431 (1994).
- [33] E. Smargiassi and P.A. Madden, Phys. Rev. B **49**, 5220 (1994).
- [34] M. Foley and P.A. Madden, Phys. Rev. B **53**, 10589 (1996).
- [35] Y.A. Wang, N. Govind, and E.A. Carter, Phys. Rev. B **58**, 13465 (1998).
- [36] Y.A. Wang, N. Govind, and E.A. Carter, Phys. Rev. B **60** (24), 16350 (1999).
- [37] L.H. Thomas, Proc. Cambridge Phil. Soc. **23**, 542 (1927).
- [38] E. Fermi, Rend. Accad. Lincei **6**, 602 (1927).
- [39] E. Fermi, Z. Phys. **48**, 73 (1928).
- [40] C.F. von Weizsäcker, Z. Phys. **96**, 431 (1935).
- [41] B. Zhou, Y.A. Wang, and E.A. Carter, Phys. Rev. B **69**, 125109 (2004).
- [42] C. Huang and E.A. Carter, Phys. Chem. Chem. Phys. **10**, 7109 (2008).
- [43] Q. Wu and W. Yang, J. Chem. Phys. **118**, 2498 (2003).
- [44] P.E. Blochl, Phys. Rev. B **50**, 17953 (1994).
- [45] G. Kresse, Phys. Rev. B **54**, 11169 (1996).
- [46] G. Kresse and D. Joubert, Phys. Rev. B **59**, 1758 (1999).
- [47] J.P. Perdew, K. Burke, and M. Ernzerhof, Phys. Rev. Lett. **77**, 3865 (1996).
- [48] D. Alfe and M.J. Gillan, Phys. Rev. B **68**, 205212 (2003).
- [49] F.D. Murnaghan, Proc. Natl. Acad. Sci. USA **30**, 244 (1944).
- [50] S. Nose, J. Chem. Phys. **81**, 511 (1984).
- [51] W.G. Hoover, Phys. Rev. A **31**, 1695 (1985).
- [52] M. Parrinello and A. Rahman, Phys. Rev. Lett. **45** (14), 1196 (1980).
- [53] G.J. Martyna, M.E. Tuckerman, D.J. Tobias, and M.L. Klein, Mol. Phys. **87** (5), 1117 (1996).
- [54] D.K. Chokappa and P. Clancy, Mol. Phys. **61** (3), 597 (1987).
- [55] B.B. Laird and A.D.J. Haymet, Chem. Rev. **92**, 1819 (1992).
- [56] D. Frenkel, Eur. Phys. J. Plus **128**, 10 (2013).
- [57] X. Gonze, B. Amadon, P.-M. Anglade, J.-M. Beuken, F. Bottin, P. Boulanger, F. Bruneval, D. Caliste, R. Caracas, M. Côté, T. Deutsch, L. Genovese, Ph. Ghosez, M. Giantomassi, S. Goedecker, D.R. Hamann, P. Hermet, F. Jollet, G. Jomard, S. Leroux, M. Mancini, S. Mazevet, M.J.T. Oliveira, G. Onida, Y. Pouillon, T. Rangel, G.-M. Rignanese, D. Sangalli, R. Shaltaf, M. Torrent, M.J. Verstraete, G. Zerah, and J.W. Zwanziger, Comp. Phys. Comm. **180**, 2582 (2010).
- [58] G. Kresse, J. Non-Cryst. Solids **205-207**, 833 (1996).
- [59] R.W. Ohse, in *Handbook of Thermodynamic and Transport Properties of Alkali Metals*, edited by Roland W. Ohse (Blackwell Science, Inc., Oxford, 1985).
- [60] H. Olbrich H. Ruppertsberg and S. Steeb, Z. Naturf. a **38**, 1328 (1983).